View metadata, citation and similar papers at core.ac.uk

brought to you by CORE

provided by Queen Mary Research Online

Modelling the Onset of Phase Separation in CaO-SiO_2-$CaCl_2$ Chlorine-Containing Silicate Glasses

Laura A. Swansbury†, Gavin Mountjoy*,†, Xiaojing Chen‡, Natalia Karpukhina‡, and Robert Hill‡

† School of Physical Sciences, University of Kent, Canterbury, Kent, CT2 7NH, U.K.

‡Dental Physical Sciences, Institute of Dentistry, Queen Mary University of London, Mile End Road, London, E1 4NS, U.K.

ABSTRACT

The addition of chlorine into a bioactive glass composition is expected to reduce its abrasiveness and increase its bioactivity, which is important for dental applications such as toothpastes. There is a lack of information and understanding regarding the structural role of chlorine in chlorine-containing bioactive silicate glasses. This has prompted classical core-shell model molecular dynamics simulations of $(50\text{-}x/2)CaO\text{-}(50\text{-}x/2)SiO_2\text{-}xCaCl_2$ glasses to be performed, where x ranges from x=0.0 to x=43.1 mol% $CaCl_2$. These ternary glasses are advantageous for a fundamental study because they do not have additional network formers (e.g. phosphorus pentoxide) or modifiers (e.g. sodium) typically found in bioactive glass compositions. The $(50\text{-}x/2)CaO\text{-}(50\text{-}x/2)SiO_2\text{-}xCaCl_2$ glasses were seen to become phase separated around the x=16.1 mol% $CaCl_2$ composition and chlorine predominantly coordinated with calcium. These findings provide a solid foundation for further computational modelling work on more complex chlorine-containing bioactive glass compositions.

INTRODUCTION

Bioactive glasses can be used as toothpaste additives to promote apatite formation and help prevent tooth hypersensitivity which affects up to 35% of the population [1]. The addition of fluorine into a bioactive glass composition causes the formation of more acid-resistant fluorapatite (FA) rather than more soluble hydroxyapatite (HA) [2]. The addition of fluorine also inhibits bacterial enzymes and promotes enamel demineralization, helping to prevent dental caries [3]. The major disadvantage of fluorine-containing bioactive glasses is that the formation of fluorite is possible [4]. Fluorite formation comes at the expense of apatite formation, potentially hindering enamel regeneration. Excessive fluorine consumption can also result in dental fluorosis [5].

Some of the limitations of fluorine-containing bioactive glasses have caused attention to turn to the possibility of using chlorine-containing bioactive glasses as an alternative [6]. Both fluorine and chlorine share similar chemical properties but the larger ionic radius of chlorine compared to oxygen is anticipated to expand the glass network [5]. This could reduce the glass transition temperature, hardness, and abrasiveness of the glass. In addition, it should result in a glass that dissolves more quickly, lessening the time required for enamel regeneration [5]. This makes chlorine-containing bioactive glasses particularly appealing for dental applications. To date, chlorine-containing silicate glasses have few applications. This is because during the melt-quench process, significant chlorine volatilization makes chlorine retention challenging [7]. An additional concern is that once prepared, glasses with high chlorine content are hygroscopic [8].

Through minimising the surface area exposed to the atmosphere in the furnace by using reagent masses of 200g, Chen [8] was able to successfully synthesize a series of chlorine-

containing bioactive glass compositions (SiO_2-CaO-P_2O_5-$CaCl_2$ with approximately 6mol% P_2O_5), as well as simpler ternary chlorine-containing oxide glasses (SiO_2-CaO-$CaCl_2$). Chen [8] noticed that the introduction of chlorine in the form of $CaCl_2$ caused a marked decrease in both the glass transition temperature and the density of the glass. These findings are consistent with an expanded network due to the larger ionic radius of chlorine compared to oxygen. Interestingly in the ternary series, a distinct break in the linear density, molar volume, and first crystallization temperature trends between the 16.1mol% and 27.4mol% $CaCl_2$ compositions were also observed. Despite this, no significant glass structure characterization was undertaken. This was partly due to ^{35}Cl MAS NMR being extremely challenging to perform [9]. The structural role of chlorine in the SiO_2-CaO-$CaCl_2$ glasses, and ultimately the glass degradation mechanisms in more complex bioactive glass compositions therefore remains unclear.

It is known that bioactive glasses typically only contain small proportions of P_2O_5. This is because it has a limited solubility in the silicate glass network, which inevitably causes crystallization with increasing phosphate content. The ubiquitous 45S5 bioactive glass developed by Larry Hench in 1960's [10] for example contained 2.6mol% P_2O_5. The fluorine-containing bioactive compositions developed by Brauer et al. [11] for dental applications contained around 1mol% P_2O_5. Another common constituent of bioactive glasses is Na_2O, but a number of sodium-free bioactive glasses have been synthesized [2,11,12].

It was therefore intuitive to study the structural role of chlorine in the simpler SiO_2-CaO-$CaCl_2$ glasses synthesized by Chen [8] prior to investigating the structure of chlorine-containing bioactive glass compositions. The challenging nature of experimentally probing the ternary (50-x/2)CaO-(50-x/2)SiO_2-x$CaCl_2$ glasses prepared by Chen [8], where x ranged

from 0.0 to 43.1mol% $CaCl_2$ prompted computational modelling using core-shell model classical molecular dynamics simulation. The results including images of the models, pair correlation functions, structure factors, and silicon network connectivity values were used for informative structural characterization.

METHODOLOGY

The nominal glass series synthesised by Chen [8] via a melt-quench technique is shown in table 1. The nominal compositions are based on an equal $CaO:SiO_2$ ratio corresponding to a calcium metasilicate and have increasing $CaCl_2$ content. The compositions were designed in this way with the expectation that the connectivity would stay constant with the $CaO:SiO_2$ ratio and that $CaCl_2$ would not behave as a network modifier. Compositional analysis of the samples involved mixing 0.60g of powdered sample with 6.00g of lithium borate flux. Fusion beads were then produced using an Eagon 2 fusion instrument. Standard fusion beads containing a series of eight well-defined $CaSiO_3$ and $CaCl_2$ mixtures were made in the same manner. X-ray fluorescence spectroscopy (XRF) measurements were then performed on half of the samples. The sample compositions were calibrated against the standards with an estimated uncertainty of $\pm$1 mol%, and small deviations from the nominal compositions were seen (table 1). As the deviations did not show any consistent trend, it was assumed that the chlorine losses via volatilization were minimal. Raman spectra of the samples were compared to the $50SiO_2$-50CaO (equal proportions of SiO_2 and CaO), the $54.29SiO_2$-45.71CaO (SiO_2 rich), and the $43.67SiO_2$-56.33CaO (CaO rich) glass spectra reported by Luth et al. [13]. These confirmed that the calcium silicate component of the glasses had equal $CaO:SiO_2$ ratios. It was therefore taken that the actual glass compositions matched the

nominal compositions. The glass densities reported by Chen [8] were identified using helium pycnometry.

Table 1: The nominal and analyzed ternary glass compositions (mol%) synthesized by Chen et al. [8] and their corresponding experimental density values. Samples not analyzed are denoted as '-'.

Nominal			Analysed			
SiO_2	CaO	$CaCl_2$	SiO_2	CaO	$CaCl_2$	Density (g/cm^3)
50.0	50.0	0.0	-	-	-	2.89
48.9	48.9	2.2	-	-	-	2.88
48.4	48.4	3.3	49.3	47.6	3.1	2.86
47.9	47.9	4.3	-	-	-	2.84
46.7	46.7	6.6	47.2	45.8	7.1	2.82
45.3	45.3	9.3	46.5	43.8	9.7	2.79
44.1	44.1	11.9	-	-	-	2.78
41.9	41.9	16.1	44.0	42.3	13.7	2.72
36.3	36.3	27.4	38.5	32.0	29.5	2.63
33.3	33.3	33.5	-	-	-	2.55
28.5	28.5	43.1	-	-	-	2.39

Classical molecular dynamics simulation (MD) with the addition of the core-shell model on the anions enables ionic polarizability to be accounted for. Most of the interatomic potential parameters required for the CaO-SiO_2-$CaCl_2$ system were obtained from Malavasi *et al.* [14] and Rabone and De Leeuw [15], but it was necessary to fit the Si-Cl interatomic potential parameter manually using the General Utility Lattice Program (GULP) [16]. The two-body core-shell model interatomic potentials of Buckingham form and the three-body interatomic potential of screened harmonic form used in this work are given in table 2.

Table 2: The two-body and three-body core-shell model interatomic potential parameters used to model SiO_2-CaO-$CaCl_2$ glass. The subscripts 'c' and 's' denote ion cores and ion shells respectively. The oxygen and chlorine shell masses used were 0.20 u and 1.50 u respectively.

Two body $V(r_{ij}) = A\exp\left(-\frac{r_{ij}}{\rho}\right) - \frac{C}{r_{ij}^6}$			
	A (eV)	ρ (Å)	C (eV Å^6)
$O_s - O_s$	22764.30	0.1490	27.88
$Si_c - O_s$	1283.91	0.32052	10.66158
$Cl_s - Cl_s$	49039.26	0.243207	16.05
$Si_c - Cl_s$	1063.00	0.3352	17.00
$Cl_s - O_s$	71379.71	0.227705	0.13
$Ca_c - Cl_s$	1220.80	0.35300	0.00
$Ca_c - O_s$	2152.3566	0.309227	0.09944
Three body $V(\theta_{jik}) = \frac{k_3}{2}(\theta_{jik} - \theta_0)^2\exp\left[-\left(\frac{r_{ij}}{\rho} + \frac{r_{ik}}{\rho}\right)\right]$			
	k_3 (eV rad^{-2})	θ_0 (°)	ρ (Å)
$O_s - Si_c - O_s$	100	109.47	1.0
Core-shell potential $V = \frac{1}{2}K_{cs}r^2$			
	K_{cs} (eV Å^{-2})	Q (core) (e)	q (shell) (e)
$O_c - O_s$	74.92	0.8482	-2.8482
$Cl_c - Cl_s$	54.41	1.650	-2.650
Si_c		4.000	
Ca_c		2.000	

Crystal structures of $CaCl_2$ [17], $CaSiO_3$ [18], $SiCl_4$ [19], $(Cl_2SiO)_4$ [20], and $Si_6O_7Cl_{10}$ [21] were used to test the performance of the interatomic potentials in table 2 using GULP[16] (table 3). The bulk crystal structures of $CaCl_2$ and $CaSiO_3$ were reproduced well, and in particular the nearest neighbour distances and coordination numbers. Although the crystal structures containing silicon and chlorine ions are molecular crystals and so more susceptible to volume change, the interatomic potentials replicated the nearest neighbour distances and coordination numbers well. They could therefore be used in the glass simulations.

Table 3: GULP results for chlorine-containing crystal structures (using P1 symmetry), where the input crystal parameters are compared with the percentage changes in the output structures (given in brackets).

	$CaCl_2$ [17]	$CaSiO_3$ [18]	$SiCl_4$ [19]	$(Cl_2SiO)_4$ [20]	$Si_6O_7Cl_{10}$ [21]
$R_{Si-O/Ca-O}$ (Å)		1.64 (-1.01)/ 2.41 (0.55)		1.58 (3.25)	1.60 (1.78)
$R_{Si-Cl/Ca-Cl}$ (Å)	2.74 (-0.13)		2.01 (-1.25)	1.99 (0.89)	2.01 (0.24)
Volume (Å^3)	168.52 (-0.26)	823.73 (-0.94)	575.73 (1.48)	392.81 (6.61)	1030.92 (13.55)
a (Å)	6.24 (0.16)	15.42 (0.13)	9.61 (-4.10)	6.17 (0.95)	6.09 (11.31)
b (Å)	6.43 (-2.85)	7.32 (1.70)	6.36 (-11.66)	8.25 (2.69)	20.68 (-1.23)
c (Å)	4.20 (3.03)	7.32 (-2.77)	9.67 (17.36)	8.34 (1.14)	8.30 (2.86)
α (°)	90.00 (0.00)	90.00 (0.00)	90.00 (-0.08)	77.31 (9.13)	90.00 (-0.47)
β (°)	90.00 (0.00)	95.37 (-0.35)	102.91 (-6.89)	80.72 (5.34)	99.47 (-1.57)
γ (°)	90.00 (0.00)	90.00 (0.00)	90.00 (-0.02)	72.67 (-1.65)	90.00 (0.00)

Each of the computational glass models contained between 10,000-11,000 atoms corresponding to box lengths of 50-60 Å. An NVT Berendsen thermostat and full equilibration was used for all simulation stages. The application of the core-shell model in simulations is known to sometimes cause instabilities (e.g. [23]), particularly at higher temperatures. It was therefore necessary to treat the higher temperature stages of the simulations as being rigid-ion (RI). The ions were therefore treated as being solid spheres without shells in these stages. Estimated RI interatomic potential parameters (table 4) based on the core-shell model interatomic potentials in table 2 were used in the RI stages. The RI stages began at 6000K to ensure a random distribution of ions. The temperature was then reduced to 3000K, and then to 2000K where it was quenched at a rate of 10^{13} K/s to 300K. The single temperature stages comprised of 400,000 time-steps and the quench stage used 170,000 time-steps, where the time-step was 1 fs. Chlorine and oxygen shells were then

added to the output configuration of atoms from the 300K RI stage, and this served as the input configuration for the core-shell model stages that followed.

Table 4: The two-body and three-body rigid-ion interatomic potential parameters used to model SiO_2-CaO-$CaCl_2$ glass. The subscript 'c' denotes ion cores.

Two body $V(r_{ij}) = A\exp\left(-\frac{r_{ij}}{\rho}\right) - \frac{C}{r_{ij}^6}$			
	A (eV)	ρ (Å)	C (eV Å^6)
$O_c - O_c$	22764.30	0.1490	27.88
$Si_c - O_c$	1283.91	0.32052	10.66158
$Cl_c - Cl_c$	49039.26	0.243207	16.05
$Si_c - Cl_c$	1063.00	0.3352	17.00
$Cl_c - O_c$	71379.71	0.227705	0.13
$Ca_c - Cl_c$	1220.80	0.35300	0.00
$Ca_c - O_c$	2152.3566	0.309227	0.09944
Three body $V(\theta_{jik}) = \frac{k_3}{2}(\theta_{jik} - \theta_0)^2 \exp\left[-\left(\frac{r_{ij}}{\rho} + \frac{r_{ik}}{\rho}\right)\right]$			
	k_3 (eV rad^{-2})	θ_0 (°)	ρ (Å)
$O_c - Si_c - O_c$	100	109.47	1.0
	Q (core) (e)		
$O_c - O_c$	-2.0000		
$Cl_c - Cl_c$	-1.000		
Si_c	4.000		
Ca_c	2.000		

The core-shell model (SM) simulations ran using the interatomic potentials in table 2. They were run using a version of the program DL POLY [22] modified to include frictional damping of shells and began at 2000K. The system was then quenched as before at a rate of 10^{13} K/s to 300K, and a further stage at 300K ensured the formation of a solid glass model. A smaller time-step of 0.1fs was necessary to follow the trajectory of the shells more closely. To compensate for the SM simulations being run with shorter time-steps, 800,000 time-steps were used in the single temperature stages. The quench stage now necessitated 1,700,000 time-steps.

As mentioned, an NVT Berendsen thermostat was used throughout to produce models with specified density. However, as often happens in classical MD of melt-quenched glasses it was not possible to match both experimental density and pressure. Tests showed that using experimental densities (table 1) resulted in high pressures at 300K of approximately 3GPa for compositions up to x=16.1 and 2GPa for x=27.4. Hence, glass models were made using density values that were equivalent to 95% of the experimental densities for compositions up to x=16.1, and 98% of the experimental density for x=27.4. Experimental density values were used for compositions beyond x=27.4.

RESULTS AND DISCUSSION

The (50-x/2)CaO-(50-x/2)SiO_2-x$CaCl_2$ glasses form a series in which $CaCl_2$ is progressively added to a calcium metasilicate base glass. For the goal of synthesizing such glasses and obtaining useful properties due to the presence of chlorine ions, it is of great relevance to understand the effect of chlorine ions on the silicate network. Figure 1 shows the Si-O, O-O, Si···Si, and Si···Ca pair correlation functions for x=0.0, 11.9, 27.4, and 43.1. The nearest neighbour peaks in these pair correlation functions correspond to short range order in the silicate component of the (50-x/2)CaO-(50-x/2)SiO_2-x$CaCl_2$ glass models. The Si-O and O-O nearest neighbour peaks correspond to SiO_4 tetrahedral units in the silicate network, and the Si···Si nearest neighbour peak coresponds to corner-linked tetrahedra. The short range order of the x=0.0 glass model is in good agreement with that expected for pure calcium metasilicate glass (the latter is described in [18]). It is striking that the nearest neighbour Si-O, O-O, Si···Si, and Si···Ca peaks show very little change even when the $CaCl_2$ content is dramatically increased up to x=43.1. This suggests that the silicate network is largely unaffected by the $CaCl_2$ content.

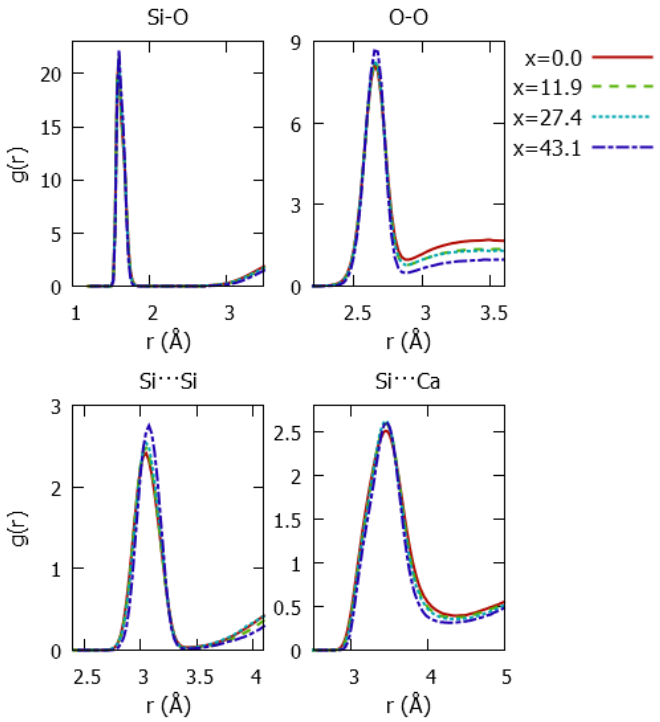

Figure 1: Si-O, O-O, Si···Si, and Si···Ca nearest neighbour peaks corresponding to the short range order in the silicate component of the (50-x/2)CaO-(50-x/2)SiO_2-x$CaCl_2$ glass models for x=0.0, 11.9, 27.4, and 43.1.

Images of the x=11.9, x=16.1, and x=27.4 computational models in figure 2 suggest that phase separation occurred around the x=16.1 composition and continued to grow with increasing $CaCl_2$ content. Viewing the separate elemental constituents of the x=16.1 and x=27.4 models in figure 3 provides further evidence that phase separation began around x=16.1. Figure 3 also confirms that phase separation was clearly evident by the x=27.4 composition and that the system was biphasic. The system had separated into a $CaSiO_3$ rich region and a $CaCl_2$ rich region. The presence of calcium in both phases explains its apparent random distribution in figure 3. Due to the limited model sizes (~53 $Å)^3$ however, the true scale of phase separation could not be identified.

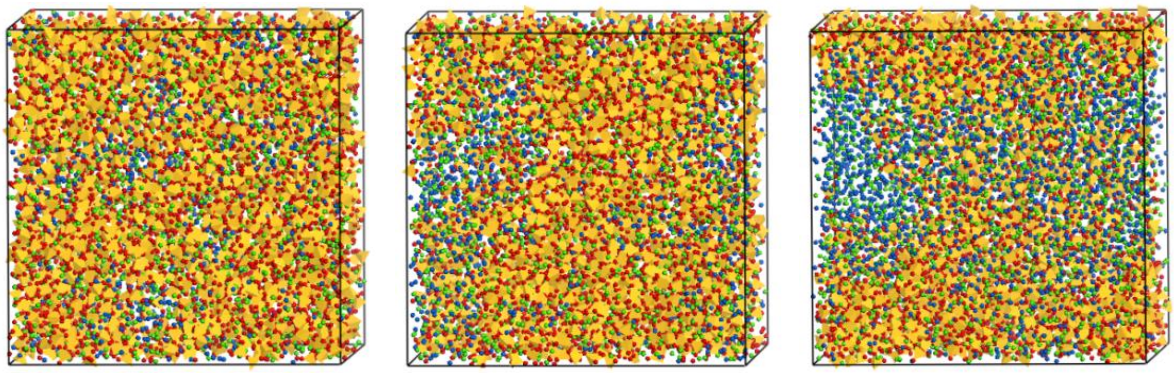

Figure 2: Images of the x=11.9, x=16.1, and x=27.4 models (from left to right respectively). The yellow tetrahedra represent silicon ions, and the red, green and blue spheres correspond to oxygen, calcium, and chlorine ions respectively.

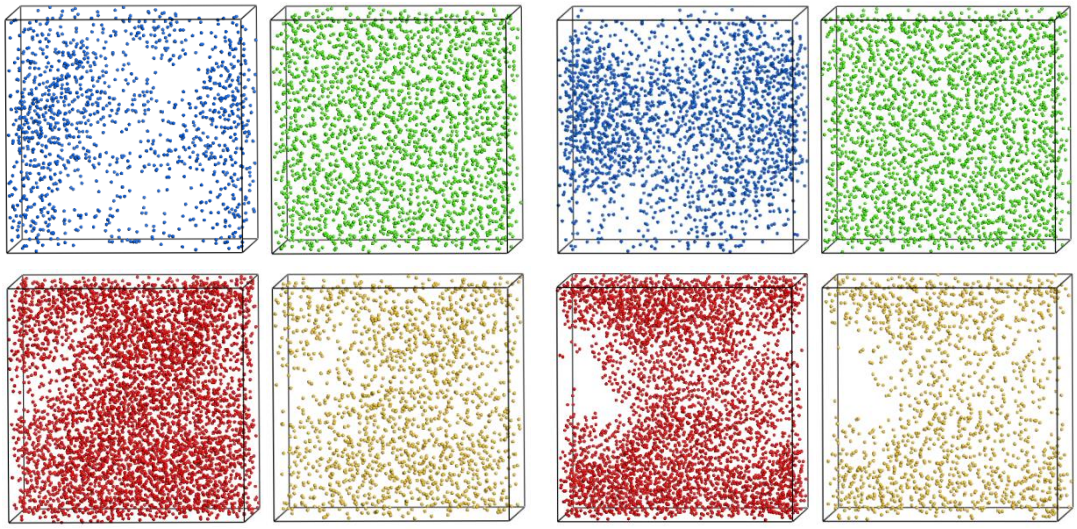

Figure 3: The distribution of chlorine (blue), calcium (green), oxygen (red) and silicon (yellow) ions in the x=16.1 (left) and x=27.4 (right) models.

Following the inspection of model images, the pair correlation functions were analysed to extract nearest neighbour distances, R, and coordination numbers, N. The values of R were identified by establishing the midpoint in the full width at half maximum (FWHM) of the first peak in the pair correlation functions. This took any peak asymmetry into account. The uncertainties in the FWHM were assigned as the uncertainties in R. Values of N were obtained by integrating the pair correlation functions and applying a cut-off distance. The

uncertainties in N were based on the sensitivity of the cumulative coordination number to small changes in the cut-off distance.

The Si-O, Si···Si, O-O, and Si···Ca nearest neighbour distances remained unchanged over the composition series with values of 1.62 ±0.01 Å, 3.06 ±0.01 Å, 2.66 ±0.01 Å, and 3.44 ±0.01 Å respectively. Through applying a cut-off distance of 2.00 Å to the Si-O correlation, a coordination number of 4.00 ±0.01 was obtained. The Si···Si coordination number varied between 2.01 and 2.06 (±0.02) when a cut-off distance of 3.40 Å was used. If on average each SiO_4 tetrahedra is corner sharing with two other tetrahedra, as in a metasilicate, then the O-O nearest neighbour coordination number is expected to be 4.00. The O-O coordination number was found to vary from 4.37 to 4.19 (±0.03) when a cut-off distance of 2.85 Å was used. The Si···Ca coordination numbers declined slightly from 6.12 to 5.39 (±0.03) because of the decreasing silicon content when a cut-off of 4.35 Å was applied.

The Ca-O nearest neighbour distances also remained unchanged over the composition series with a value of 2.36 ±0.01 Å. The Ca-O coordination number decreased with increasing $CaCl_2$ content due to the declining oxygen contribution. The values ranged from 6.14 to 2.24 (±0.03) when cut-off distances of 3.10 Å were used. Details of the remaining correlations are presented in table 5. It can be seen that the Ca···Cl nearest neighbour distance of approximately 2.8 Å corresponds to Ca···Cl bonds associated with the $CaCl_2$ phase of the $(50-x/2)CaO-(50-x/2)SiO_2-xCaCl_2$ glass models. The Ca···Cl coordination numbers increased with increasing $CaCl_2$ content due to the increasing contribution from chlorine ions. Coordination number values ranged from 0.36 to 4.22 when a cut-off of 3.70 Å was used.

Table 5: The nearest neighbour distance, R, and coordination number, N, values for the Ca···Cl, Cl···Cl, Cl···O, Ca···Ca, and Si···Cl correlations. Cut-off distances of 3.70 Å, 4.90 Å, 4.70 Å, 5.25 Å, and 5.65 Å were applied to attain the coordination numbers respectively.

	Ca···Cl		Cl···Cl		Cl···O		Ca···Ca		Si···Cl	
x	R ±0.01Å	N ±0.05	R ±0.05 Å	N ±0.10	R ±0.10 Å	N ±0.10	R ±0.05 Å	N ±0.05	R ±0.10 Å	N ±0.10
0.0							3.90	7.47		
2.2	2.81	0.36	3.55	1.04	3.78	15.15	3.93	7.55	4.59	0.87
3.3	2.81	0.52	3.54	1.85	3.79	13.76	3.97	7.63	4.60	1.22
4.3	2.81	0.67	3.57	2.50	3.79	12.96	4.05	7.61	4.61	1.52
6.6	2.80	0.99	3.59	3.54	3.80	11.49	4.11	7.63	4.63	2.10
9.3	2.79	1.33	3.61	4.84	3.79	9.59	4.20	7.63	4.65	2.58
11.9	2.78	1.62	3.63	5.72	3.77	8.40	4.37	7.72	4.62	2.96
16.1	2.78	2.08	3.65	6.97	3.78	6.57	4.48	7.72	4.63	3.44
27.4	2.77	3.20	3.61	9.40	3.77	3.64	4.56	8.25	4.61	3.70
33.5	2.77	3.68	3.62	9.88	3.75	3.00	4.60	8.41	4.63	3.75
43.1	2.77	4.22	3.73	9.52	3.79	2.99	4.69	8.08	4.67	5.72

The Si···Cl nearest neighbour distances of approximately 4.6 Å (table 5 and figure 4) means there was no Si···Cl bonding. The chlorine ions did not bond with silicon ions in the models. This clearly contrasts with the shorter Ca···Cl nearest neighbour distances of ~2.8 Å (table 5) which confirmed that chlorine ions bond with calcium ions.

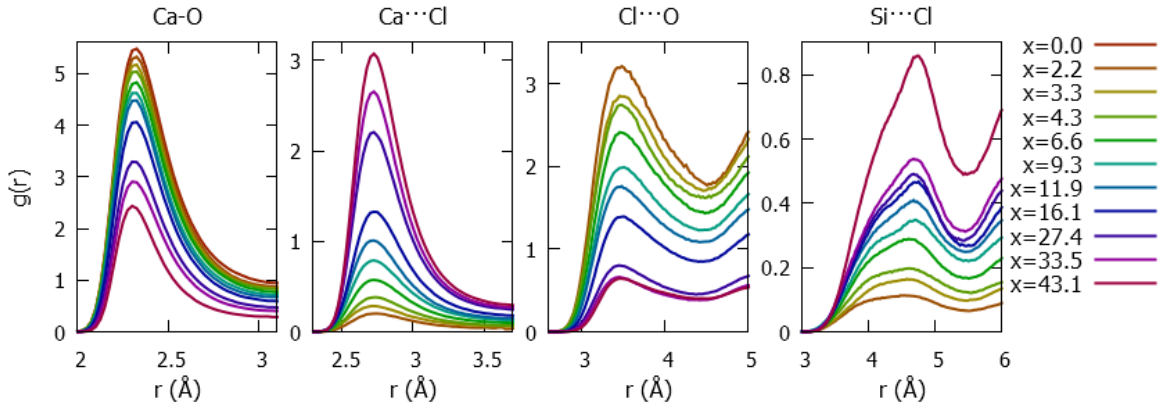

Figure 4: The Ca-O, Ca···Cl, Cl···O, and Si···Cl pair correlation functions for the compositions in table 1. The g(r) amplitude decreases with increasing $CaCl_2$ content for Ca-O and Cl···O, and increases with increasing $CaCl_2$ content for Ca···Cl and Si···Cl.

It can be seen in table 5 that the Cl···Cl and Ca···Ca separation distances generally increase with increasing $CaCl_2$ content. This highlights the tendency towards phase separated $CaCl_2$ and $CaSiO_3$ regions even in the compositions of low $CaCl_2$ content. Whilst most pair correlation function plots exhibited a consistent shape over the composition range, examining the Ca···Ca pair correlation functions (figure 5) more closely reveals a distinct change with varying $CaCl_2$ content. The most noticeable change in shape occurred between the x=16.1 and the x=27.4 compositions, the point at which Chen [8] noticed a distinct change in density, molar volume, and first crystallization temperature experimentally. For glass compositions of low $CaCl_2$ content, the $CaSiO_3$ phase dominates and so Ca···Ca nearest neighbour distances correspond more closely with those in crystalline $CaSiO_3$ (3.65 Å [24]). As the $CaCl_2$ content increases, the $CaCl_2$ phase becomes increasingly dominant and so the Ca···Ca nearest neighbour distances increase and become more comparable to those in crystalline $CaCl_2$ (4.20 Å [17]). In the two crystalline structures, the Ca···Ca nearest neighbours are separated by anions. The smaller oxygen anions in crystalline $CaSiO_3$ gives smaller Ca···Ca nearest neighbour distances compared to the larger chlorine anions in crystalline $CaCl_2$. Calculating the Ca···Ca nearest neighbour distances in the glasses yields distances of 3.93 Å and 4.60 Å for the x=2.2 and x=33.5 compositions respectively. These values are noticeably greater than those in crystalline $CaSiO_3$ and $CaCl_2$ respectively, but the calculations account for the asymmetry in the peaks due to the disorder in the glass.

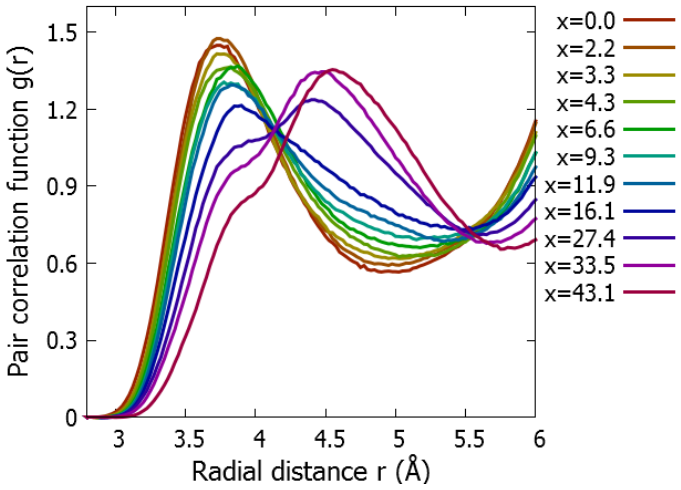

Figure 5: The Ca···Ca pair correlation functions for the compositions in table 1. The plots are shown from left to right for low to high $CaCl_2$ content respectively.

The simulated total neutron and x-ray structure factors ($S_N(K)$ and $S_X(K)$) in figure 6 also exhibited changes with composition. These changes were predominantly caused by the Cl···Cl, Cl···O, and O-O partial structure factors. This reflects the changing elemental contributions because as the chlorine content is increased, the oxygen content gets reduced (table 1). The sharp vertical lines at small scattering vector values seen in the plots to the right of figure 6 on the scale of 0.2 to 0.6 $Å^{-1}$ are indicative of inhomogeneity, or phase separation and begin in the x=16.1 composition. The range of scattering vector values (ΔK) for which sharp vertical lines are seen is related to the scale (L) of phase separation via $L \sim 2\pi/\Delta K$ [25]. This gives L~20 Å, although this may not be the true scale of phase separation due to the limited model sizes.

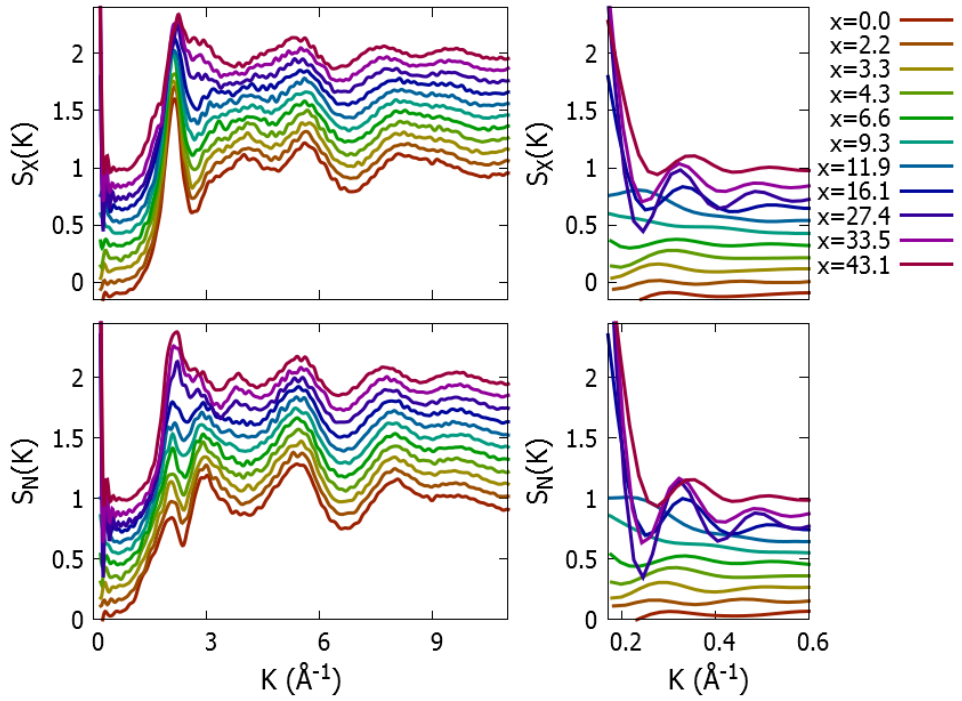

Figure 6: Simulated total x-ray ($S_x(K)$) and neutron ($S_N(K)$) structure factor spectra for the compositions in table 1. The plots to the left cover scattering vector (K) magnitudes from 0.00 to 10.00 while the plots to the right cover K values from 0.17 to 0.60. The plots are progressively offset from x=0.0 by 0.1 upwards.

Comprehending the network connectivity is fundamental in identifying the rate at which a bioactive glass will degrade when inserted into the body. A value in the region of 2.00 is often ideal [10]. The connectivity values in this study were predicted using the equation y=-2x+8 where the terms y and x denote the connectivity and the O:Si ratio respectively. This gives a connectivity (y) of 2.00 for an equal $CaO:SiO_2$ ratio corresponding to a metasilicate. The actual connectivity values from the models were in good agreement with both the predicted values (table 6) and experimental NMR data [6]. It can be noticed that the connectivity values in the most phase separated glass models are marginally higher. This is due to a slight and increasing content of 'free' oxygens, but the explanation for this is unclear.

Table 6: The silicon network connectivity distribution alongside the average and predicted values.

x	Si atoms	Q^0 (%)	Q^1 (%)	Q^2 (%)	Q^3 (%)	Q^4 (%)	Average Q^n	Predicted Q^n
0.0	2000	1.55	22.90	50.80	23.45	1.30	2.00	2.00
2.2	1956	1.64	23.01	50.41	23.47	1.48	2.00	2.00
3.3	1936	1.19	22.52	52.89	21.59	1.81	2.00	2.00
4.3	1912	1.52	23.27	50.58	22.75	1.88	2.00	2.00
6.6	1868	1.50	22.16	53.05	21.47	1.82	2.00	2.00
9.3	1812	1.60	22.41	51.43	23.29	1.27	2.00	2.00
11.9	1764	1.53	22.11	52.78	21.66	1.93	2.00	2.00
16.1	1676	2.09	22.26	50.89	22.55	2.21	2.00	2.00
27.4	1452	2.89	21.49	48.07	25.21	2.34	2.03	2.02
33.5	1332	2.63	22.45	45.12	27.40	2.40	2.05	2.04
43.1	1140	3.77	20.00	47.02	26.58	2.63	2.04	2.04

Regarding future computational work, it would be of interest to simulate the addition of P_2O_5 and/or Na_2O into the ternary SiO_2-CaO-$CaCl_2$ glass compositions. Experimentally, small angle neutron scattering (SANS) and small angle x-ray scattering (SAXS) experiments should be considered to probe the scale of phase separation.

CONCLUSIONS

The expected properties of chlorine-containing bioactive glasses could make them ideally suited to dental applications. However, a current lack of structural understanding regarding the role of chlorine in particular prevents these glasses from being utilized. This study investigated the structure of a SiO_2-CaO-$CaCl_2$ glass series as a foundation to ultimately understanding both the structure and degradation mechanisms of chlorine-containing bioactive glasses. The SiO_2-CaO-$CaCl_2$ glass series maintained equal CaO:SiO_2 ratios and the $CaCl_2$ content ranged from 0.0 to 43.1 mol%. Classical molecular dynamics with core-shell model interatomic potentials was used to make models containing 10,000-11,000 atoms corresponding to box lengths of 50-60 Å.

In all models there was an absence of Si-Cl bonding. Instead, the Ca···Cl nearest neighbour distances of ~2.8 Å elucidated that chlorine ions bond with calcium ions. Over the entire glass series the Ca···Cl bonding had minimal impact on the silicon network connectivity and this was consistent with a metasilicate. Upon increasing the $CaCl_2$ content to around 16 mol%, the emergence of a $CaSiO_3$ rich phase and a $CaCl_2$ rich phase started to become apparent. This could be seen in the inhomogeneous distributions of the silicon, oxygen, and chlorine ions, with an approximate scale of phase separation being around 20 Å (although, this may not be the true scale of phase separation due to the limited model sizes). This phase separation continued to proliferate with increasing $CaCl_2$ content. There was also a marked effect on the Ca···Ca nearest neighbour distances. These were shorter for low $CaCl_2$ contents where the $CaSiO_3$ rich phase was dominant and the calcium ions were separated by oxygen ions. For $CaCl_2$ contents above 16 mol%, there was a marked contribution of larger Ca···Ca nearest neighbour distances due to the $CaCl_2$ rich phase in which calcium ions were separated by larger chlorine ions.

ACKNOWLEDGEMENTS

The authors are grateful to EPSRC for funding, and to A. Tilocca for technical advice.

REFERENCES

(1) Jones, J. R. Reprint of: Review of Bioactive Glass: From Hench to Hybrids. *Acta Biomater.* **2015**, *23* (S), S53–S82.

(2) Mneimne, M.; Hill, R. G.; Bushby, A. J.; Brauer, D. S. High Phosphate Content Significantly Increases Apatite Formation of Fluoride-Containing Bioactive Glasses. *Acta Biomater.* **2011**, *7* (4), 1827–1834.

(3) Jabbarifar, S. E.; Salavati, S.; Akhavan, A.; Khosravi, K.; Tavakoli, N.; Nilchian, F. Effect of Fluoridated Dentifrices on Surface Microhardness of the Enamel of Deciduous Teeth. *Dent. Res. J. (Isfahan).* **2011**, *8* (3), 113.

(4) Chen, X.; Chen, X.; Brauer, D. S.; Wilson, R. M.; Hill, R. G.; Karpukhina, N. Novel Alkali

Free Bioactive Fluorapatite Glass Ceramics. *J. Non. Cryst. Solids* **2014**, *402*, 172–177.

(5) Chen, X.; Karpukhina, N.; Brauer, D. S.; Hill, R. G. Novel Highly Degradable Chloride Containing Bioactive Glasses. *Biomed. Glas.* **2015**, *1* (1), 108–118.

(6) Chen, X.; Karpukhina, N.; Brauer, D. S.; Hill, R. G. High Chloride Content Calcium Silicate Glasses. *Phys. Chem. Chem. Phys.* **2017**, *19*, 7078–7085.

(7) Kiprianov, A. A.; Karpukhina, N. G. Oxyhalide Silicate Glasses. *Glas. Phys. Chem.* **2006**, *32* (1), 1–27.

(8) Chen, X. Novel Halide Containing Bioactive Glasses, Queen Mary University of London, 2015.

(9) Baasner, A.; Hung, I.; Kemp, T. F.; Dupree, R.; Schmidt, B. C.; Webb, S. L. Constraints on the Incorporation Mechanism of Chlorine in Peralkaline and Peraluminous Na_2O-CaO-Al_2O_3-SiO_2 Glasses. *Am. Mineral.* **2014**, *99* (8–9), 1713–1723.

(10) Jones, J.; Clare, A. *Bio-Glasses: An Introduction*; John Wiley & Sons, 2012.

(11) Brauer, D. S.; Karpukhina, N.; O'Donnell, M. D.; Law, R. V.; Hill, R. G. Fluoride-Containing Bioactive Glasses: Effect of Glass Design and Structure on Degradation, pH and Apatite Formation in Simulated Body Fluid. *Acta Biomater.* **2010**, *6* (8), 3275–3282.

(12) Goel, A.; Kapoor, S.; Tilocca, A.; Rajagopal, R. R.; Ferreira, J. M. F. Structural Role of Zinc in Biodegradation of Alkali-Free Bioactive Glasses. *J. Mater. Chem. B* **2013**, *1* (24), 3073.

(13) Luth, R. W. Raman Spectroscopic Study of the Solubility Mechanisms of F in Glasses in the System CaO-CaF_2-SiO_2. *Am. Mineral.* **1988**, *73*, 297–305.

(14) Malavasi, G.; Pedone, A.; Menziani, M. C. Study of the Structural Role of Gallium and Aluminum in 45S5 Bioactive Glasses by Molecular Dynamics Simulations. *J. Phys. Chem. B* **2013**, *117* (15), 4142–4150.

(15) Rabone, J. A. L.; De Leeuw, N. H. Interatomic Potential Models for Natural Apatite Crystals: Incorporating Strontium and the Lanthanides. *J. Comput. Chem.* **2006**, *27* (2), 253–266.

(16) Gale, J. D. GULP: A Computer Program for the Symmetry-Adapted Simulation of Solids. *J. Chem. Soc. Faraday Trans.* **1997**, *93* (4), 629–637.

(17) Busing, W. R. An Interpretation of the Structures of Alkaline Earth Chlorides in Terms of Interionic Forces. *Trans. Am. Crystallogr. Assoc.* **1970**, *6*, 57–72.

(18) Ohashi, Y. Polysynthetically-Twinned Structures of Enstatite and Wollastonite. *Phys. Chem. Miner.* **1984**, *10* (5), 217–229.

(19) Zakharov, L. N.; Antipin, M. Y.; Struchkov, Y. T.; Gusev, A. V.; Gibin, A. M.; Zhernenkov, N. V. Molecular and Crystal Structures of $SiCl_4$ at 163 K. *Kristallografiya* **1986**, *31*, 171–172.

(20) Wannagat, U.; Bogedain, G.; Schervan, A.; Marsmann, H. C.; Brauer, D. J.; Buerger, H.; Doerrenbach, F.; Pawelke, G.; Krueger, C.; Claus, K. H. Das Isosterenpaar SiO/PN,I. Zur Isosterie von Perchlorcyclophosphaze Schwingungsspektren Und Roentgenstruktrukturanalyse von $(Cl_2SiO)_3$ Und $(Cl_2SiO)_4$. *Zeitschrift fuer Naturforschung, B Chem. Sci.* **1991**, *46*, 931–940.

(21) Binnewies, M.; Magull, J. Crystal Structure of Decachloro-bicyclo(5.5.1) Heptaoxatridecasilane, $Si_6O_7Cl_{10}$. *Zeitschrift fuer Krist. - New Cryst. Struct.* **2002**, *217*, 325–326.

(22) Smith, W.; Forester, T. R. DL_POLY_2. 0: A General-Purpose Parallel Molecular Dynamics Simulation Package. *J. Mol. Graph.* **1996**, *14* (3), 136–141.

(23) Tilocca, A.; De Leeuw, N. H.; Cormack, A. N. Shell-Model Molecular Dynamics Calculations of Modified Silicate Glasses. *Phys. Rev. B - Condens. Matter Mater. Phys.* **2006**, *73*, 1–14.

(24) Ohashi, Y. Polysynthetically-Twinned Structures of Enstatite and Wollastonite. *Phys. Chem. Miner.* **1984**, *10*, 217–229.

(25) Elliott, S. R. *Physics of Amorphous Materials*, Second Edi.; Longman Scientific & Technical, 1990.

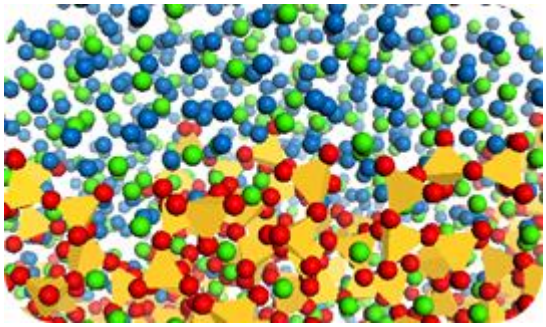

Table of Contents Graphic